Compact diode-laser spectrometer ISOWAT for highly sensitive airborne measurements of water-isotope ratios

C. Dyroff · D. Fütterer · A. Zahn

Abstract The tunable diode-laser absorption spectrometer ISOWAT for airborne measurements of the water-isotope ratios $^{18}O/^{16}O$ and D/H is described. The spectrometer uses a distributed feedback (DFB) diode laser to probe fundamental rovibrational water-absorption lines at around 2.66 µm. Very-low-noise system components along with signal averaging allow for a detection limit of 1.2 and 4.5‰ for measurements of $^{18}O/^{16}O$ and D/H, respectively, for a water-vapour mixing ratio of 100 ppmv and an averaging time of 60 s. This corresponds to a minimum detectable absorbance of $\sim 5 \times 10^{-6}$ or $\sim 6.6 \times 10^{-10}$ cm^{-1} when normalized to pathlength. In addition to its high sensitivity, the spectrometer is highly compact (19-inch rack at a height of 35 cm, excluding pump and calibration unit) and light weight (<40 kg total). The total power consumption is around 350 W, and the instrument is fully automated. ISOWAT will be calibrated during flight with known water-isotope ratios using a compact calibration-gas source.

PACS 07.57.Ty · 42.62.Fi · 42.68.Ca

1 Introduction

Water (H_2O) is one of the most important molecules in the Earth's atmosphere. It causes $\sim 2/3$ of the natural greenhouse effect of 33 K, and it transports huge amounts of latent heat. It is thus the key player in the energetic budget of

the atmosphere [1–3]. H_2O is also involved in many important homogeneous and heterogeneous chemical reactions in both the troposphere and the stratosphere. It is for instance the major source of OH radicals in the troposphere, which is by far the most important oxidant for most organic and inorganic pollutants and compounds.

In spite of the large relevance of H_2O for climate and chemical processing, the hydrological cycle from the Earth's surface up to the mesosphere is not sufficiently well understood. Examples are the transport processes and pathways that carry H_2O into the stratosphere or the extremely complex and multifaceted formation and fate of clouds and precipitation. In this respect, note that the atmospheric H_2O ($\sim 13 \times 10^{15}$ kg) is on average exchanged completely about every nine to ten days [4] and that its highly dynamic transport is linked to that of other atmospheric constituents as well [2].

Isotope-ratio measurements constitute a complementary and very powerful proxy to study various processes in which atmospheric H_2O is involved [5, 6]. The isotope ratio R of a molecular species is generally expressed as the mixing ratio of the less abundant isotopologue relative to that of the most abundant isotopologue, e.g. $R(^{18}O) = H_2^{18}O/H_2^{16}O$. Because the natural variation is generally small, these ratios are expressed in per mille (‰) relative deviation to a reference material. The internationally accepted reference material for H_2O is the Vienna Standard Mean Ocean Water (VSMOW). Further standards, such as SLAP (Standard Light Antarctic Precipitation) or GISP (Greenland Ice Sheet Precipitation) can be used to achieve a higher accuracy [7]. For the oxygen isotopologue $H_2^{18}O$, this deviation is

$$\delta^{18}O = \left(\frac{R(^{18}O)_{\text{sample}}}{R(^{16}O)_{\text{reference}}} - 1 \right) 1\,000‰. \quad (1)$$

C. Dyroff (✉) · D. Fütterer · A. Zahn
Research Centre Karlsruhe, Institute of Meteorology and
Climate Research, Hermann-von-Helmholtz-Platz 1,
76344 Eggenstein-Leopoldshafen, Germany
e-mail: Christoph.Dyroff@imk.fzk.de
Fax: +49-7247-824742

A negative δ-value therefore indicates a sample that is depleted in the less abundant isotopologue relative to the reference material.

The major source of atmospheric water vapour is the ocean. Evaporation from the ocean leads to a depletion of the heavy isotopologues (negative δ-values) in the vapour above the ocean due to the vapour pressure isotope effect (VPIE), i.e. the lower vapour pressure of e.g. $H_2^{18}O$ compared to $H_2^{16}O$. The VPIE is strongly temperature dependent and results in δD-values that are a factor of $\sim$8 more negative than those of $\delta^{18}O$. For example, at an ocean temperature of 20°C, the H_2O vapour just above the ocean shows $\delta^{18}O \approx -12‰$ and $\delta D \approx -80‰$ [1].

The second fractionation process in the troposphere, the kinetic fractionation, is due to the mass-dependent diffusion constants of the H_2O isotopologues. It occurs during the evaporation from the ocean (and other water surfaces) and the formation of cloud particles, in particular at low temperatures [8].

Condensation of the vapour leads to the formation of cloud droplets and ice particles, and the remaining vapour phase is further depleted in heavy isotopologues. The removal of cloud droplets and ice particles by precipitation yields a vapour phase increasingly depleted in heavy isotopologues (more negative δ-values) with time. The magnitude of this so called Rayleigh fractionation is specific to, e.g. large-scale ascent or convective events that leave different isotopic signatures of the H_2O vapour.

In the troposphere, all dominant fractionation processes occur in a mass-dependent manner, i.e. changes in $\delta^{18}O$ are around 2 times larger than in $\delta^{17}O$ or $\Delta^{17}O = \delta^{17}O - 0.528\,\delta^{18}O \equiv 0$ [9]. In the stratosphere, the isotopic composition is in addition modified by chemical reactions that usually result in mass-independent fractionation with $\Delta^{17}O \neq 0$.

Furthermore, there is a strong source of H_2O originating from the oxidation of methane (CH_4) and, to a lesser extent, molecular hydrogen (H_2) [10] which almost double the H_2O mixing ratio in the mesosphere. As both CH_4 and H_2 are enriched in deuterium (D) relative to H_2O imported from the troposphere, the δD values are found to be higher (less negative) with increasing altitude above the tropopause [11].

Despite their usefulness as transport tracers, measurements of atmospheric H_2O-isotope ratios have scarcely been performed in the past. Zahn et al. [6] and Franz et al. [12] have employed cryogenic trapping of water vapour in the upper troposphere and lower stratosphere with subsequent laboratory-based isotope-ratio determination by mass spectrometry. While mass spectrometry can provide high precision measurements (depending on amount of sampled H_2O, $\delta^{18}O \approx 2$–3‰ possible [12]), cryogenic trapping requires rather long sampling times ($\geq$20 min) in dry conditions. This reduces the spatial resolution of the measurement due to the high speed of the aircraft, and small spatial structures such as isolated clouds can not be resolved.

Recently, there have been a number of reports on H_2O-isotope ratio profiles deduced from satellite data [5, 10, 11, 13, 14]. While satellite data can provide the global picture, their spatial resolution is limited, allowing only to study large-scale processes.

Only very few instruments have been employed aboard aircraft to perform in-situ measurements of H_2O-isotope ratios. Webster and Heymsfield [15] used a tunable-diode laser spectrometer (TDLAS) [16] based on wavelength-modulation spectroscopy employing a (non-resonant) multi-pass-absorption cell. Both a group at the University of Groningen [17, 18] and at Harvard University [19, 20] have used instruments based on cavity-enhanced spectroscopy, where resonant cavities are used to achieve very long effective absorption pathlengths of several kilometres. St. Clair et al. [21] have employed an instrument based on the detection of the fluorescence of photolytically excited H_2O, which, however, only allows for measurements of δD. The above instruments were able to provide good quality data with high precision. With the exception of [16] and [17] they are, however, relatively large and heavy [22]. Furthermore, the instruments have only been employed for a very small number of airborne campaigns.

Our objective was to develop a compact and lightweight TDLAS system which can easily and often be deployed aboard different aircraft for in-situ measurements of the H_2O-isotope ratios $\delta^{18}O$ and δD. The instrument is highly sensitive and capable to deliver both precise and accurate measurements of $\delta^{18}O$ and δD. Furthermore, the instrument is designed to be operated in a fully unattended mode and makes use of frequent in-situ calibration. With these specifications, the ISOWAT instrument described in the present paper is planned to be operated aboard the CARIBIC (Civil Aircraft for the Regular Investigation of the atmosphere Based on an Instrument Container) passenger aircraft [23] for monthly intercontinental flights. In addition, ISOWAT will be employed aboard the new German HALO (High Altitude and LOng range) research aircraft for two upcoming campaigns (see Sect. 4). These campaigns are devoted to investigate mid-latitude cirrus clouds as well as the trace gas composition below the late winter Arctic stratospheric vortex.

2 Spectrometer design

Our goal was to design a TDLAS instrument as small and as lightweight as possible without trading off of its high-sensitivity potential.

2.1 Absorption line selection

The measurement of $\delta^{18}O$ and δD isotope ratios requires probing of one absorption line for each of the water isotopologues $H_2^{16}O$, $H_2^{18}O$ and HDO. For ISOWAT the selection of suitable absorption lines was constrained by several factors:

(1) The absorption lines should have a high integrated line strength to achieve high sensitivity. At the same time all three absorption lines should yield similar absorption at typical isotope abundances.
(2) All absorption lines should be in close spectral proximity in order to employ a single laser scan, and they should be free of relevant spectral interference with other absorbers such as CO_2, N_2O and CH_4.
(3) Furthermore, they should have similar ground-state energies in order to minimize potential thermal uncertainties due to temperature drifts.
(4) In order to avoid cryogenic cooling of laser and detectors and the accompanying bulky dewars, thermoelectrically cooled laser and detectors should be available. This would in turn also allow for a compact and lightweight design.

According to the HITRAN database [24], suitable spectral regions for isotope-ratio measurements of water vapour are found (a) in the combination band in the near infrared at around $7\,183\ \mathrm{cm}^{-1}$ ($1.39\ \mu m$) [17, 25], (b) in the fundamental band in the mid infrared around $3\,700\ \mathrm{cm}^{-1}$ ($2.7\ \mu m$) [26, 27] and (c) in the fundamental band in the mid infrared at around $1\,485\ \mathrm{cm}^{-1}$ ($6.7\ \mu m$) [15, 19]. Kerstel et al. [17] were able to achieve high sensitivity in the near infrared ($7\,183\ \mathrm{cm}^{-1}$) using a resonant cavity with a high effective optical pathlength. While most of the above criteria are met, the integrated linestrength of these absorption lines is too low to achieve the necessary sensitivity with our non-resonant approach. Absorption lines in the fundamental band around $1\,485\ \mathrm{cm}^{-1}$ provide high integrated line-strengths, but both lasers and detectors require cryogenic cooling. Due to the bulkiness of the required dewars these lines could not be selected for ISOWAT.

Based on the above criteria (1)–(4) we have identified three absorption lines near $\nu = 3\,765\ \mathrm{cm}^{-1}$ from the HITRAN database. The closest relevant absorbers are CO_2 and N_2O. Figure 1 shows a calculated spectrum of 10 ppmv H_2O as well as 380 ppmv CO_2 and 0.33 ppmv N_2O according to conditions in the tropopause region. Using simulated spectra we have determined the expected errors due to changes in CO_2 by 10% [28] and N_2O by as much as 50% [29, 30]. In this manner we determined a maximum error of around 14‰ for both $\delta^{18}O$ and δD, which is mainly due to changes in the N_2O-mixing ratio. These expected errors are generally within the measurement uncertainties of the present instrument at a water-mixing ratio of 10 ppmv.
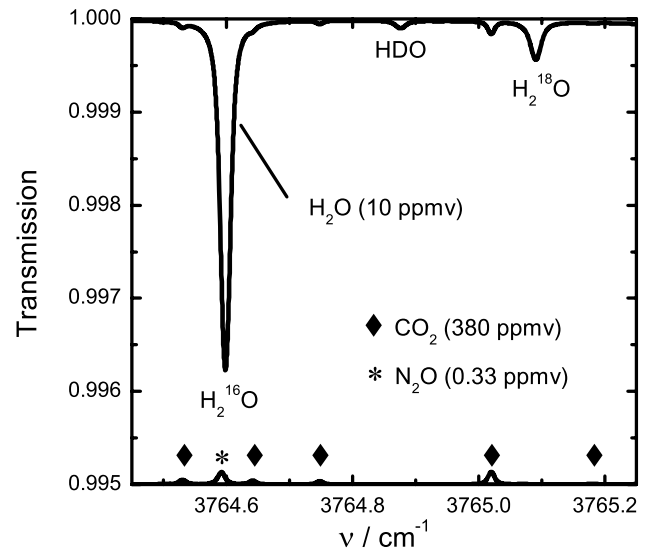
Fig. 1 Calculated transmission spectrum of a gas mixture containing 10 ppmv H_2O, 380 ppmv CO_2 and 0.33 ppmv N_2O at a pressure of 70 hPa and an absorption pathlength of 76 m. The symbols at the bottom mark the absorption features of CO_2 (♦) and N_2O (∗)

At this wavelength we can use low noise, thermoelectrically cooled detectors as well as a low-noise laser that is operated near room temperature, i.e. cryogenic cooling can be avoided. The probed absorption lines are listed in Table 1 along with their line-centre position ν_0, integrated linestrength S_{ij}, pressure-broadening coefficient in air γ_C and ground-state energy E''. Due to the low abundance of HDO, the HDO-absorption line in particular needs to be as strong as possible, and the selected line at $3\,764.88\ \mathrm{cm}^{-1}$ provides the highest integrated linestrength for the spectral window between $2\,500$ and $4\,500\ \mathrm{cm}^{-1}$.

The temperature dependence of the integrated linestrength ε_T (Table 1) has been calculated for a constant pressure using the approximation given by Giafrani et al. [25, 31]

$$\varepsilon_T = \left(\frac{T_0}{T}\right)^{5/2} \exp\left[-hc\frac{E''}{k_B}\left(\frac{1}{T} - \frac{1}{T_0}\right)\right]. \qquad (2)$$

Here, h is the Planck constant, c is the speed of light and k_B is the Boltzmann constant. From the calculated ε_T we can deduce a temperature-induced shift of the isotope-ratio measurements of $\delta_T^{18}O = -13.6‰\,K^{-1}$ and $\delta_T D = -12.2‰\,K^{-1}$. As our set-up controls the gas temperature to within $\sigma = 0.02$ K over several hours, this temperature-induced shift is generally lower than our measurement accuracy.

2.2 Optical set-up

As depicted in Fig. 2, the beam of a distributed feedback (DFB) diode laser is collected by a $f = 25.4$ mm

Table 1 Absorption lines probed and their integrated linestrength S_{ij}, air-broadening coefficient γ_C, ground-state energy E'' and temperature dependency of linestrength ε_T. The temperature coefficients ε_T have been calculated for a temperature change of 1 K around 313 K using (2). The corresponding temperature-induced shift of the isotope ratios is given as δ_T

	ν_0 (cm^{-1})	S_{ij} (cm/molecule)	γ_C (cm^{-1}/bar)	E'' (cm^{-1})	ε_T (‰/K)	δ_T (‰/K)
$H_2^{16}O$	3 764.599 13	9.347×10^{-22}	0.069 7	931.237	5.7	
$H_2^{18}O$	3 765.090 81	8.715×10^{-23}	0.101 5	0.000	−7.9	−13.6
HDO	3 764.876 29	1.648×10^{-23}	0.091 5	91.330	−6.6	−12.2
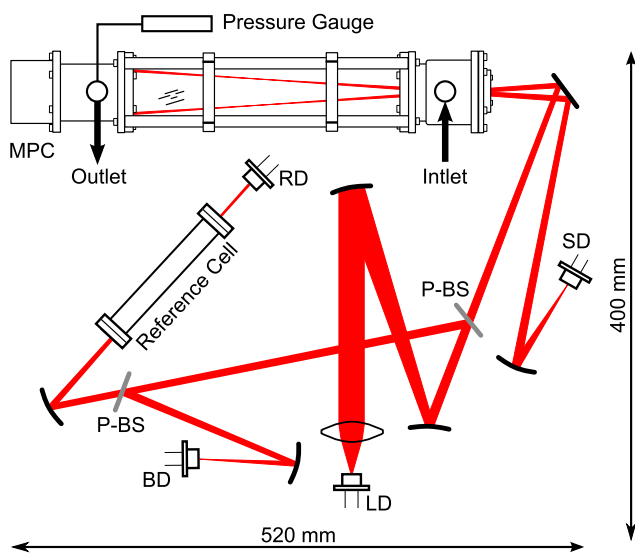
Fig. 2 Schematic of the ISOWAT optics with the beam of the laser diode (LD) depicted in red. The sample detector (SD) records spectra that are due to absorption within the multi-pass cell (MPC). A pellicle-beam splitter (P-BS) is used to pick off a fraction of the laser beam that is split in two parts by a second P-BS. The background detector (BD) is used to record spectra due to residual water absorption outside the MPC. The reference detector (RD) records H_2O spectra from within the reference cell which are used for line locking. The alignment of the optics is done with a red aiming laser (not shown). The gas inlet and outlet ports of the MPC are indicated. The pressure within the MPC is measured at the outlet port of the cell

anti-reflection-coated CaF$_2$ lens. It is then focused into an astigmatic-mirror multi-pass-absorption cell (MPC, Aerodyne Inc., USA, volume 0.5 l, base length ∼32 cm) by means of a Galileo-type telescope consisting of a $f = 300$ mm and a $f = -120$ mm spherical mirror. The beam enters the MPC within the horizontal plane through a coupling hole in the centre of the front mirror. The astigmatism of the mirrors leads to a Lissajous pattern on both mirrors as the laser beam is reflected [32]. After 238 passes (76 m absorption path) within the MPC the beam exits the cell through the same coupling hole, but at the inverted angle with respect to the optical axis of the cell. Upon exiting the MPC, the beam is focused onto the sample detector (SD) by means of a $f = 100$ mm mirror.

A fraction of 8% of the laser power is picked off using a pellicle-beam splitter (P-BS) upstream of the MPC. This beam is further split in two parts of equivalent power by a second P-BS. The transmitted beam is first guided through a reference cell filled with a high concentration of H_2O vapour and then focused onto the reference detector (RD) by a $f = 300$ mm spherical mirror. The reflected beam is focused onto the background detector (BD) using a $f = 100$ mm spherical mirror. All detectors are slightly tilted to avoid back reflection of laser radiation.

We use a custom made single mode GaInAsSb-GaSb double quantum-well DFB-diode laser (nanoplus GmbH, Germany) to probe three absorption lines around $\nu = 3765$ cm^{-1} ($\lambda = 2.66$ μm) within a single wavelength scan [33]. The laser is mounted in a TO8 package fitted with an anti-reflection coated CaF$_2$ window in order to minimize back reflection of laser radiation into the laser chip. The laser is thermoelectrically operated at around 32°C. Its output power is around 6 mW. The laser-emission frequency can be tuned by around 10 cm^{-1} (∼7 nm) by changing the laser temperature. It can furthermore be tuned by around 2 cm^{-1} (∼1.4 nm) by adjusting the laser-injection current. Both SD and BD are thermoelectrically cooled photovoltaic HgCdTe detectors operated at −70°C. The RD, which is less demanding in terms of signal-to-noise ratio, is a thermoelectrically cooled photovoltaic InSb detector operated at −40°C.

The spectrometer optics are mounted on a 40×52 cm^2 aluminium breadboard. The breadboard is mounted on vibration-damping elements in a closed compartment on top of the spectrometer's electronics compartment (Fig. 5). The instrument housing is based on a rugged and lightweight aluminium frame (Enviscope GmbH, Germany), which takes the main mechanical load. The instrument is enclosed by lightweight, aluminium-coated honeycomb material. In contrast to the electronics compartment (lower part of the instrument), the optics compartment is temperature stabilized to 40 ± 0.1°C. The MPC is temperaturized by separate heaters to 40 ± 0.02°C in order to maximize the system stability. The pressure within the multi-pass cell is maintained at $p_{MPC} = 70$ hPa. No desiccants are used to remove ambient

water vapour from the optics compartment, and the compartment pressure is not stabilized.

2.3 Data acquisition and handling

For our isotope-ratio measurements we apply wavelength-modulation spectroscopy [34, 35]. A digital-signal processing (DSP) computer provides a sawtooth-voltage ramp at a frequency $f_{ramp} = 10$ Hz (Fig. 3), which is fed into a low-noise laser driver (ITC102, Thorlabs GmbH, Germany). This laser driver also controls the temperature of the laser to $\sim 32°$C.

In addition to the ramp, the laser-injection current is sinusoidally modulated at a frequency $f_{mod} = 57$ kHz. The detector signals are demodulated at twice the modulation frequency ($2 f_{mod}$) by means of analog lock-in amplifiers (LIA-BVD-150-H, Femto GmbH, Germany). This results in absorption spectra that are similar to the second derivative of the direct absorption spectra. The amplitude of the sinusoidal-modulation waveform corresponds to ~ 2.2 times the half width at half maximum (HWHM) of the absorption lines in order to achieve the maximum second-derivative signal [36].

In this manner we record three sets of second-derivative spectra:

(1) The reference spectra originating from the absorption within the reference cell are measured by the reference detector (RD, Fig. 2), demodulated at $2 f_{mod}$ by a lock-in amplifier and finally read by the DSP computer. The
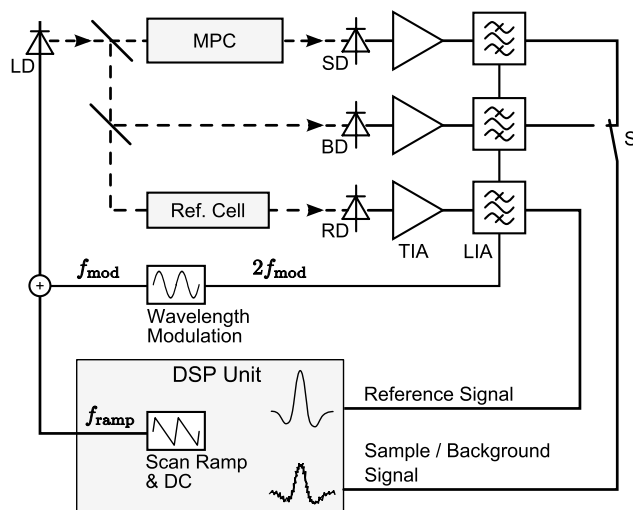
Fig. 3 Schematic of the ISOWAT data acquisition system with LD: laser diode, MPC: multi-pass cell, SD: sample detector, BD: background detector and RD: reference detector. The detector signals are amplified by transimpedance amplifiers (TIA) and demodulated at $2 f_{mod}$ by lock-in amplifiers (LIA) yielding second-derivative spectra. Switch S is used to alternate between sample and background signal. The ambient spectra are achieved by subtracting the background spectra from the sample spectra

peak position of the $H_2^{16}O$ line is determined by means of a parabolic fit. The difference between the actual peak position and the pre-defined position is fed back for each wavelength scan as DC offset to the laser injection current in order to compensate for potential wavelength drift.

(2) The sample spectra originating from absorption within the MPC are recorded by the sample detector (SD) and subsequently demodulated at $2 f_{mod}$ by a lock-in amplifier.

(3) We furthermore measure spectra that are due to absorption of water vapour within the spectrometer and outside of the MPC. These background spectra are detected by the background detector (BD) and also demodulated at $2 f_{mod}$ by a lock-in amplifier.

Even though the absorption lines of H_2O at cabin pressure ($p = 800 \ldots 1\,000$ hPa) are substantially broadened, the generally high water-mixing ratio in the cabin of above $\sim 5\,000$ ppmv leads to a $2 f_{mod}$ signal that can not be neglected. We thus regularly measure and subtract the background spectra from the sample spectra. This is done by our DSP computer after switching from the SD signal to the BD signal (switch S in Fig. 3). In the laboratory, a BD spectrum (30 s average) is recorded after every calibration, whereas on the aircraft we will also take BD measurements in between calibrations to account for potential faster changes of H_2O in the cabin. Simultaneous recording of SD and BD spectra is currently not possible due to the limited number of input channels of our DSP board.

A typical measurement sequence starts with the recording of a calibration spectrum. To this end, the MPC is first flushed with a calibration-gas of known H_2O-mixing ratio and isotopic composition for 60 s. The calibration standard is provided by a calibration-gas source as described below. A high signal-to-noise ratio calibration spectrum is then recorded with an averaging time of 30 s. The subsequent 30 s are used to (a) flush the MPC with sample air for the following sample measurements and (b) record a 30 s average background spectrum (by switching switch S, Fig. 3). Thereafter sample air is measured at an averaging time of 1 s for 10 min after which the next calibration measurement starts.

In order to determine the isotope ratios $\delta^{18}O$ and δD, the spectra are first split in three parts, each of which only contains the respective signal of the $H_2^{16}O$, $H_2^{18}O$ and HDO absorption line (see Fig. 4). As a second step, we apply singular-value decomposition (SVD), a common technique in linear algebra, inter alia, to apply least-squares fitting of data [27, 37]. The fit considers four individual terms: (i) the $2 f_{mod}$ signal, (ii) a DC baseline offset, (iii) a linear baseline slope and (iv) a quadratic baseline bend. The latter terms are included in order to compensate for potential baseline distortions that would otherwise lead to erroneous fit results. For each term, a scaling factor W of
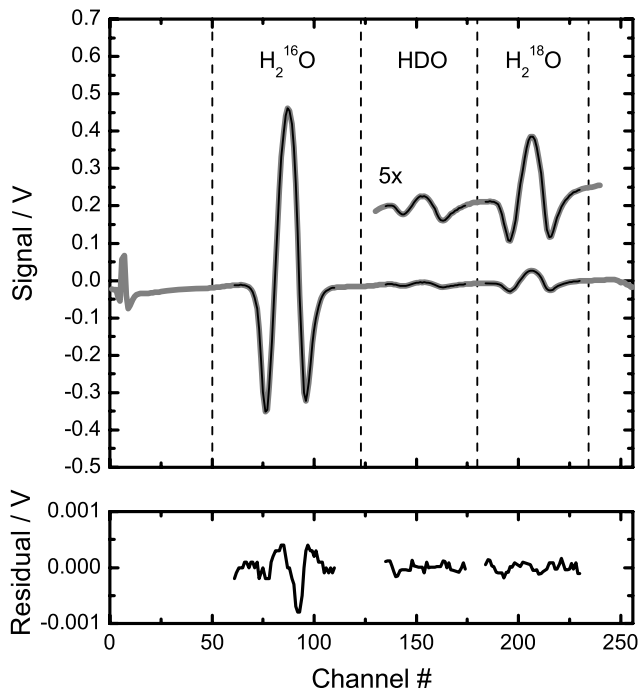
Fig. 4 Second-derivative spectrum (*thick gray trace*) of the three water isotopologues $H_2^{16}O$, HDO and $H_2^{18}O$ probed around $3\,765$ cm^{-1} (1 s average). The H_2O-mixing ratio was 160 ppmv. The inset shows a $5\times$ enlargement of the HDO and $H_2^{18}O$ absorption lines. The spike at the left side of the spectrum is due to the rapid change in the sawtooth-scan ramp. The *thin black lines* indicate the corresponding fit, and the residuals are shown in the *lower panel*

the current ambient spectrum with respect to the previously recorded calibration spectrum is determined such that the sum of the four components represents best the calibration spectrum. For a mathematical treatment we refer to the description by Werle et al. [37]. Figure 4 depicts a measured spectrum (grey trace) at a water-mixing ratio of around 160 ppmv. The fit to this particular spectrum is given as thin black trace, and the residuals are shown in the lower panel.

For the calculation of the isotope ratios we only consider the scaling factor of the $2f_{mod}$ signal, i.e. the relative concentration of the individual isotopologues with respect to the calibration spectrum. For $H_2^{16}O$ this is defined as

$$W\left(H_2^{16}O\right) = [c](H_2^{16}O)_{Amb}/[c]\left(H_2^{16}O\right)_{Cal}, \quad (3)$$

where $[c](H_2^{16}O)_{Amb}$ and $[c](H_2^{16}O)_{Cal}$ denote the mixing ratio of $H_2^{16}O$ during ambient and calibration measurement, respectively. For conditions found in the upper troposphere and lower stratosphere, these measurements are not affected considerably by the non-linearity of Beer–Lambert's law.

Recalling the definition of the isotope ratio (1), and performing minor rearrangements we determine e.g. $\delta^{18}O$ by

solving

$$\delta^{18}O = \left[\frac{([c]H_2^{18}O/[c]H_2^{16}O)_{Amb}}{([c]H_2^{18}O/[c]H_2^{16}O)_{Cal}} - 1\right] \cdot 1\,000\%_0$$

$$= \left[\frac{W(H_2^{18}O)}{W(H_2^{16}O)} - 1\right] \cdot 1\,000\%_0. \quad (4)$$

It is worth noting that no calibration in terms of absolute mixing ratio for any of the isotopologues is necessary for isotope-ratio measurements. However, we do calibrate the instrument with a known water-mixing ratio and isotopic composition. In the future we also want to determine the water vapour mixing ratio from the fit of the $H_2^{16}O$ absorption signal. Until then we need to perform further tests to evaluate the long-term stability of our calibration source.

2.4 Calibration

In order to calibrate the spectrometer during flight, we have developed a compact calibration unit that provides a calibration-gas standard of known humidity and isotopic composition.

Inflowing air is first dried by pumping it (using a small membrane pump) through four parallel stainless steel cartridges containing molecular sieve with a pore width of 0.3 nm as desiccant. The cartridges have a diameter of 12.7 mm (0.5 in) and a length of 40 cm. Using this approach, the residual water-mixing ratio of the dried air is below 3 ppmv at ambient air mixing ratios of up to $15\,000$ ppmv. CO_2 is also partially removed by the molecular sieve, however, the changes to the absorption spectra (Fig. 1) are negligible. We have performed long-term tests using a water-mixing ratio of $5\,000$ ppmv generated by a bubbler source. This humidity is at least a factor of 10 higher than what is measured on average on an intercontinental flight with the CARIBIC aircraft at 10–12 km altitude [23], where the water-mixing ratio generally spans between around 5 ppmv when the aircraft flies through the lowermost stratosphere to around $5\,000$ ppmv during ascent and descent of the aircraft. Under these conditions, the dryer nevertheless provided air with $[c](H_2O) < 4$ ppmv for more than 24 hours.

The dried air is then split into two flows by means of two mass-flow controllers (MFC). A small flow of $1 \ldots 10 \times 10^{-3}$ slpm [1 slpm = $1\,000$ cm^3 at $1\,000$ hPa and 20°C per minute] is guided through a custom designed stainless-steel bubbler, which is filled with our calibration standard, i.e. water of known isotopic composition. There, the air flow is humidified to 100% relative humidity. This humidified air is then diluted into the main dry-air flow of 2 slpm. The pressure within the bubbler is equal to the pressure in the exhaust line of the aircraft, i.e. around ambient pressure between $1\,000$ hPa at ground level and 200 hPa at an altitude

of $\sim$12 km. The MFC has thus to be controlled (depending on pressure) to provide a constant mixing ratio of 300 ppmv.

The water vapour evaporated within the bubbler unit is depleted in the isotopologues $H_2^{18}O$ and HDO with respect to the liquid phase due to their slightly lower vapour pressure [8, 38]. This fractionation depends only on the temperature during evaporation [1], because of which we control the bubbler temperature to $T = 40 \pm 0.02°C$. This increased temperature has two advantages. Firstly, the depletion of the heavy isotopologues in the vapour phase decreases with increasing temperature during evaporation. Secondly, as a consequence of the smaller depletion, the (unavoidable) temporal drift of the isotopic composition of the calibration standard due to the shrinking liquid reservoir is also reduced.

The chosen temperature of 40°C leads to an isotopic composition of the evaporated water vapour of $\delta^{18}O = -12‰$ and $\delta D = -60‰$ [1, 39] with respect to the liquid phase. The flow of 10×10^{-3} slpm through the bubbler diluted into the dry-air (<3 ppmv) flow of 2 slpm at a pressure of 1000 hPa yields a calibration gas with a water-mixing ratio of $\sim$300 ppmv. At these conditions, the liquid-water reservoir of 10 ml would last for $\sim$500 hours. During evaporation of the first half (250 hours) the drift of the isotopic composition of the vapour phase is only about $\Delta(\delta^{18}O) \approx 1.5‰$/ml and $\Delta(\delta D) \approx 7‰$/ml. This drift is considered during operation even though it remains in the order of the uncertainty of our isotope-ratio measurements at a water-mixing ratio of 300 ppmv.

2.5 Gas flow system

The two inlet ports of the spectrometer are connected to the sample-air inlet (total water, i.e. gas phase and cloud particles) and to the calibration-gas source (Fig. 5) by electropolished stainless-steel tubing. A three-way solenoid valve located in the lower part of the spectrometer switches between the two air flows. It is followed by a proportional valve that maintains a constant pressure of $p_{MPC} = 70$ hPa within the multi-pass cell. The gas pressure inside the MPC is measured using a high-precision absolute-pressure gauge (PMP-4000, GE-Sensing, USA) which is connected to the outlet port of the MPC (see Fig. 2).

Water is a highly polar molecule and thus is adsorbed to any surface. In order to minimize its exchange with sample air in the inlet lines, all tubing upstream of the MPC is made of electro-polished stainless steel. Both the tubing and the MPC are further heated to 40°C because the water adsorption strongly decreases with increasing temperature. The sample-gas flow rate of $\sim$1.5 slpm through the MPC is established by a membrane pump, which is connected to the outlet port of the spectrometer. A 1.6 l buffer volume located upstream of the pump minimizes pressure fluctuations within the MPC, which might be induced by the pump.

Downstream of the MPC only Teflon tubing is used to reduce weight. Solenoid valves are closed to seal off the instrument when not in use in order to avoid contamination with (mostly humid) ambient air.
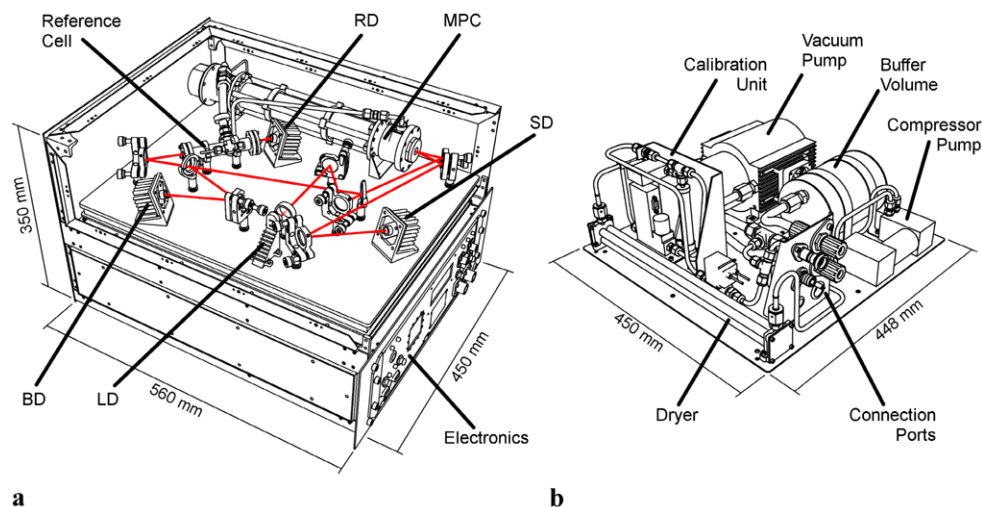
Fig. 5 (**a**) Isometric view of the ISOWAT H_2O-isotope ratio spectrometer (some parts of the enclosure as well as the aiming laser are not shown for better illustration). The instrument is designed as a 19-inch subrack, and its weight is around 27 kg. The electronics and valves are located in the lower half of the instrument. The optics are mounted in the upper half in a separate and temperaturized compartment. The

laser-beam path is depicted as *red trace*. The gas-connection ports are located at the rear of the instrument (not shown). (**b**) Isometric view of the compact assembly comprising the calibration unit and the pumps (around 12 kg). Spectrometer and calibration unit are connected by stainless steel (calibration gas) and Teflon (pump) tubing (not shown here)

3 Spectrometer performance

Laboratory tests have been performed to quantify the spectrometer's important parameters, such as gas exchange, sensitivity and accuracy. The detection limit was determined by means of the Allan-variance method. The accuracy was evaluated by measuring two largely different working standards of known isotopic composition.

3.1 Gas exchange

With the flow rate of 1.5 slpm and the MPC pressure of 70 hPa, the response of the spectrometer to a rapid change between two working standards (GW-9 and AIC-48, see Table 2) with largely different isotopic composition was measured (Fig. 6). A fast time constant of around 10 s and a long time constant of around 100 s was determined using a double-exponential fit. At an aircraft speed of around

Table 2 Actual accuracy of ISOWAT at 600 ppmv and 100 ppmv evaluating 60 s averages

		$[c]$/ppmv	$\delta^{18}O$/‰	δD/‰
GW-9	IRMS		-9.02 ± 0.03	-62.7 ± 0.4
	ISOWAT	600	-8.6 ± 1.1	-61.4 ± 11.2
	ISOWAT	100	-10.5 ± 3.6	-60.2 ± 9
AIC-48	IRMS		-47.71 ± 0.06	-381.1 ± 3.1
	ISOWAT	600	-46.5 ± 1.4	-381.4 ± 12.6
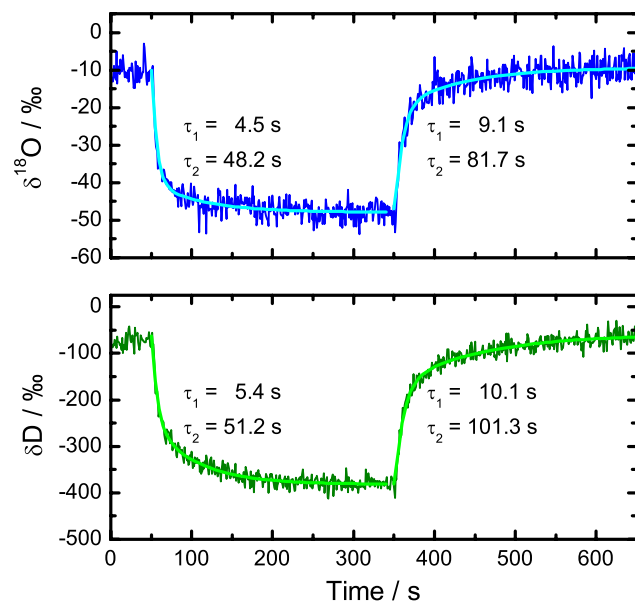
Fig. 6 Exchange-time measurements with the two working standards GW-9 and AIC-48. The *thick solid lines* show results of a double-exponential fit indicating a fast exchange time of around 10 s and a slow exchange time of around 100 s

250 m/s, the 10 s exchange time results in a maximum horizontal resolution of around 2.5 km.

The fast exchange time is around a factor of 6 higher than the theoretical air exchange time of the MPC and upstream tubing of ~ 1.4 s. The larger time constant for the isotopologues is most likely due to adsorption/desorption effects of the MPC and upstream tubing walls. In addition, the small volume at the rear end of the MPC, which contains the mechanical assembly for alignment of the MPC optics, is at present not well flushed. An additional flow port will be added to this volume to maximize the gas exchange throughout the MPC volume. An even shorter exchange time would require a bigger pump, which did not meet the stringent size and weight requirements for the present spectrometer.

3.2 Detection limit

To quantify the detection limit, the spectrometer was first calibrated with a gas mixture having a H_2O-mixing ratio of 100 ppmv and our GW-9 working standard calibrated by isotope-ratio mass spectrometry (IRMS) having an isotopic composition of $\delta^{18}O = -9.02$‰ and $\delta D = -62.7$‰ with respect to VSMOW [40].

The gas mixture was produced by diluting saturated water vapour from a bubbler at 30°C into a flow of dry air. After recording a 30 s average calibration spectrum, the spectrometer measured the same calibration gas mixture for 600 s at a 1 Hz detection bandwidth (Figs. 7a and b). The measured isotope ratios $\delta^{18}O$ and δD were then analyzed in terms of the Allan variance. Thereby, the time series data are split in m samples of length τ with the corresponding mean value $A_i(\tau)$. As explained by Werle et al. [37], the Allan variance σ^2_{Allan} is defined as the mean squared deviation of adjacent averages

$$\sigma^2_{Allan}(\tau) = \frac{1}{2m} \sum_{i=1}^{m} \left[A_{i+1}(\tau) - A_i(\tau) \right]^2. \tag{5}$$

It is generally plotted as a function of τ in a log-log plot. For statistically independent measurements, σ^2_{Allan} decreases proportional to τ. Drift in the time series, however, reduces this decrease, and σ^2_{Allan} is no longer reduced beyond a certain optimum averaging time τ_{opt}. Beyond τ_{opt} the deviation of the adjacent averages and thus σ^2_{Allan} increases. Such drift is e.g. seen in the $\delta^{18}O$ measurements (Fig. 7a) at ~ 1.25 h, where the isotope ratio decreases by around 10..15‰ within 10 min. The following step back to the former isotope ratios is due to a new calibration.

For actual measurements we compare the adjacent calibration spectra and perform a linear interpolation over time, which is a good approximation over a 10 min measurement. This minimizes the effects of systematic drift. However, for
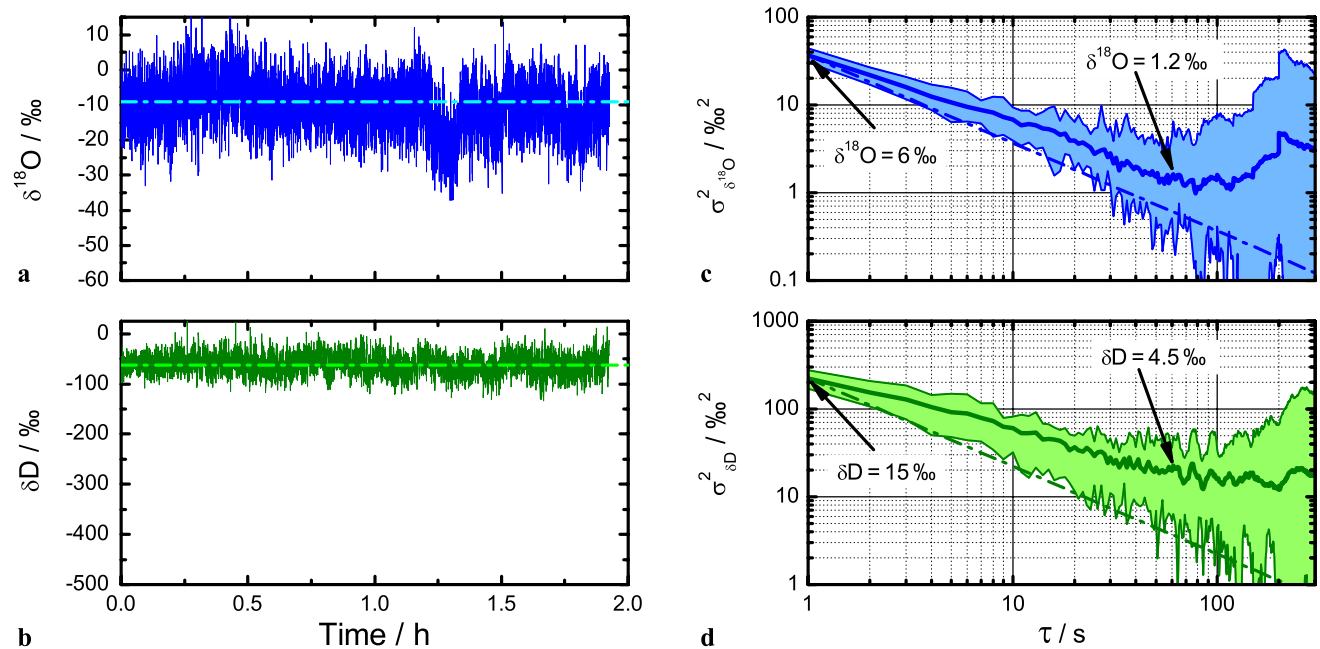
Fig. 7 Time series of (**a**) δ^{18}O and (**b**) δD isotope-ratio measurements of the GW-9 working standard at a 1 Hz detection bandwidth and a total water-mixing ratio of 100 ppmv. The *dashed horizontal lines* indicate the isotope ratios as determined by IRMS. The same ordinate scale as in Fig. 8 is chosen for better comparison. (**c**) Corresponding Allan variance σ^2_{Allan} versus averaging time τ for measurements

of δ^{18}O and (**d**) δD. The *thick solid traces* depict the average Allan variance for 11 consecutive measurements, and the *shaded areas* mark the minimum and maximum boundaries for these measurements. The *dashed lines* indicate the theoretical behaviour for statistically independent measurements

the Allan-variance analysis we did not apply linear interpolation as we wanted to investigate the magnitude of systematic drift.

Figures 7c and d show the Allan variance σ^2_{Allan} versus averaging time τ for δ^{18}O and δD, respectively, for a laboratory test as described above. The thick traces show the average Allan variance for 11 consecutive measurement sequences of 600 s each, and the shaded areas mark the minimum and maximum. The straight dashed lines show the expected behaviour for statistically independent measurements, where σ^2_{Allan} decreases proportional to τ. As can be seen, this behaviour was met for at least one of the 11 measurement sequences for averaging times of 300 s.

Based on Fig. 7 we derived the detection limit (precision) of the present instrument at 100 ppmv. At 1 s averaging time the precision is found to be δ^{18}O = 6‰ and δD = 15‰. Averaging for 60 s improves the detection limit to δ^{18}O = 1.2‰ and δD = 4.5‰. Based on the H_2^{16}O absorption line, the corresponding minimum detectable line centre absorbance for 60 s averaging time was determined to be $\sim 5 \times 10^{-6}$ or $\sim 6.6 \times 10^{-10}$ cm^{-1} when normalized to pathlength.

While the minimum boundary for both δ^{18}O and δD measurements falls onto the theoretical line for statistically independent measurements (dashed lines), the average Allan variance lays above this line. This can be attributed to sys-

tematic drift of the spectrometer, which is due to time dependent etalon signals superimposed onto the spectra. The somewhat stronger drift observed in the δD-Allan plot is attributed to the lower HDO signal relative to the underlying etalon signal. The etalon signals could be assigned to unwanted interference of scattered light within the multi-pass cell. Even very small temperature changes of the MPC cause relevant changes of the phase of the etalon signal. This in turn leads to a drift in the determined concentrations and isotope ratios over time. As seen in Fig. 7, at $\tau = 60$ s σ^2_{Allan} is increased on average by around a factor of 2–3 due to systematic drift, and thus the sensitivity is reduced by around a factor of 1.5.

3.3 Accuracy

The accuracy of the spectrometer was evaluated by measuring the isotopic composition of two largely different working standards. These standards were:

(1) Local groundwater (GW-9) with δ^{18}O = -9.02 ± 0.03‰ and δD = -62.7 ± 0.4‰.
(2) Water from an Antarctic ice core (AIC-48) with δ^{18}O = -47.71 ± 0.06‰ and δD = -381.1 ± 3.1‰

with respect to VSMOW [40].

A gas mixture containing a mixing ratio of 600 ppmv was produced in two separate bubblers that were operated at

30°C. At this temperature, fractionation during evaporation in the bubbler leads to a further isotope depletion of both gas mixtures [1], yielding final values of $\delta^{18}O = -22.02‰$ and $\delta D = -131.8‰$ for the GW-9 standard, as well as $\delta^{18}O = -60.71‰$ and $\delta D = -450.2‰$ for the AIC-48 standard.

The measurement procedure consisted of three sequences (S1 to S3) that were repeated 22 times. In S1, the instrument was first calibrated with the ground-water standard (GW-9) for 30 s. In S2, this standard was measured again for the following 60 s at a 1 Hz detection bandwidth. The corresponding 60 s average constituted the first sample measurement. Then we switched to the Antarctic standard (AIC-48) and allowed for sufficient exchange time of ~3 min. In the following sequence S3, AIC-48 was measured for 60 s which constituted the second sample measurement. S1 to S3 lasted for around 10 min and were repeated 22 times.

Figure 8 depicts the 60 s average measurements for both $\delta^{18}O$ and δD with respect to VSMOW along with their standard deviations as error bars. Also shown as dashed lines are the actual values for both working standards as determined by IRMS.

The mean value of the 22 measurements of the GW-9 standard are $\delta^{18}O = -8.6 \pm 1.1‰$ and $\delta D = -61.4 \pm 11.2‰$ with respect to VSMOW. The deviation of the mean from the actual values is $\delta^{18}O_{dev} = 0.4‰$ and $\delta D_{dev} = 1.3‰$. For the AIC-48 standard we measure on average $\delta^{18}O = -46.5 \pm 1.4‰$ and $\delta D = -381.4 \pm 12.6‰$ with a deviation from the actual values of $\delta^{18}O_{dev} = 1.2‰$ and $\delta D_{dev} = -0.3‰$. As indicated in Table 2, the $\delta^{18}O$ and δD
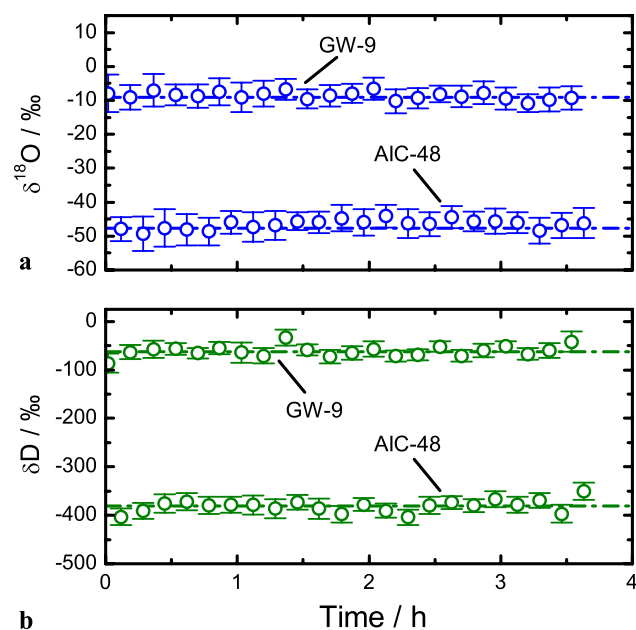
Fig. 8 Time series of 22 consecutive isotope-ratio measurements of $\delta^{18}O$ (**a**) and δD (**b**) of the two different working standards GW-9 and AIC-48 (indicated as *dashed lines*). The error bars indicate the standard deviation of the individual 60 s averages

values measured by ISOWAT are for both standards within the 2σ-standard deviation identical with the actual values.

As a comparison to the measurements at 600 ppmv we have also evaluated the 11 measurements of the GW-9 standard at 100 ppmv (Fig. 7) with respect to the measurement accuracy. For averages over 60 s we find $\delta^{18}O = -10.5 \pm 3.6‰$ and $\delta D = -60.4 \pm 9‰$. The deviation from the expected values of $\delta^{18}O_{dev} = -1.5‰$ and $\delta D_{dev} = 2.3‰$ is also insignificant and within the 2σ-standard deviation.

We note that the standard deviation (σ) of the individual 60 s measurements at 100 ppmv is a factor of around 2–3 higher than what was determined from the Allan-variance analysis at an averaging time of 60 s (Fig. 7). This is due to the fact that the Allan variance is a measure of short-term precision as it is defined as the mean-squared deviation of adjacent averages of averaging time τ (5). The classical variance (σ^2), however, is defined as the mean-squared deviation of the individual measurements x_i to the ensemble average μ [$\sigma^2 = \overline{(x_i - \mu)^2}$]. In the case of (slow) drift, the deviation of adjacent averages can be smaller than the deviation to the ensemble average and consequently $\sigma^2_{Allan} < \sigma^2$.

3.4 Upper-tropospheric conditions

We have furthermore tested ISOWAT at rapid humidity variations between ~40 ppmv and 1 000 ppmv as encountered in the upper troposphere (UT). In contrast to the UT we supplied the spectrometer with water vapour of constant isotopic composition (GW-9). The time series of the H_2O-mixing ratio is shown in Fig. 9a. Due to the constant isotopic composition one would expect constant isotope-ratio measurements, i.e. $\delta = 0$ relative to the calibration value, with increasing noise at lower mixing ratios. However, our measurements reveal changes in the determined δ-values as depicted in Fig. 9b. The plot shows the 1 s measurements of δD versus $\delta^{18}O$, where the color code represents the H_2O-mixing ratio of the particular measurement. The mean values of all measurements were determined to be $\delta^{18}O = 19.02 \pm 26.45‰$ and $\delta D = 7.5 \pm 33.5‰$, i.e. within 1σ identical with the expected $\delta = 0$, but a significant offset in $\delta^{18}O$ appears at H_2O-mixing ratios below 100 ppmv.

Repeated dynamical measurements of the kind have shown comparable results, but reveal no evidence for a systematic behavior, i.e. negative or positive offset at certain H_2O-mixing ratios. We attribute this behaviour to the changing residual spectral baseline (etalon signal). At present our fit algorithm is unable to fully capture this phenomenon, but we will address this in future work. In conclusion we estimate the accuracy of our spectrometer to be ~50‰ for both $\delta^{18}O$ and δD at rapidly varying H_2O-mixing ratios prevailing in the UT.

In general, drift of the residual spectral background, which is caused by unwanted interference within the MPC
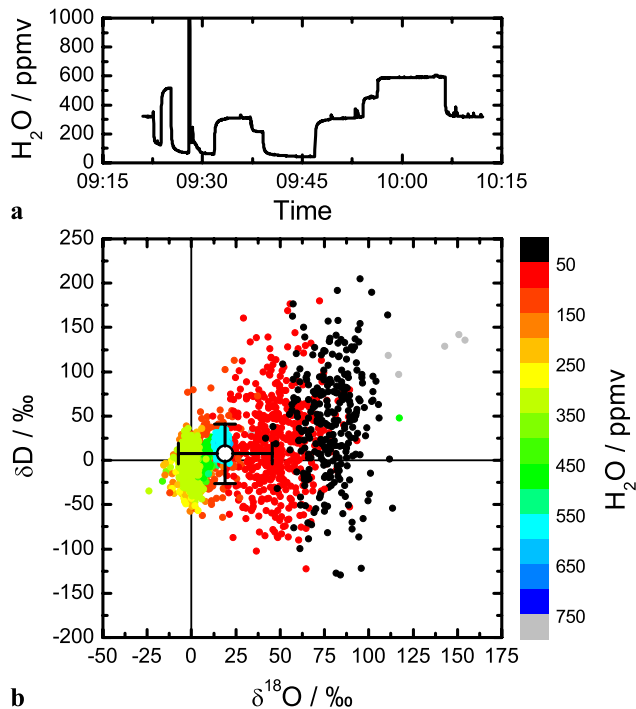
Fig. 9 (**a**) Time series of H_2O-mixing ratio with random variation between $\sim$40 ppmv and >1 000 ppmv. (**b**) Measurements of $\delta^{18}O$ and δD relative to calibration values at 1 s averaging time as a response to the variation of the H_2O-mixing ratio depicted in (**a**). The color code indicated the mixing ratio for the individual measurements. The *circle* represents the mean value of all measurements and the *error bars* give the standard deviation. The mean values of $\delta^{18}O = 19.02 \pm 26.45\permil$ and $\delta D = 7.5 \pm 33.5\permil$ are within 1σ equal to zero

and HDO around 3 765 cm^{-1} are probed with a low-noise laser that is operated near room temperature. Both careful electrical engineering and advanced signal processing contribute to the high signal-to-noise ratio achieved.

We have determined the precision of the present spectrometer using the Allan-variance method. For a total water-mixing ratio of 100 ppmv a precision of $\delta^{18}O = 6\permil$ and $\delta D = 15\permil$ was determined for an averaging time of 1 s. For 60 s averaging time the precision is improved to $\delta^{18}O = 1.2\permil$ and $\delta D = 4.5\permil$. This corresponds to a minimum detectable absorbance of $\sim 5 \times 10^{-6}$ for 60 s averaging time.

The accuracy of ISOWAT at 600 ppmv was measured to be better than $2\permil$ for $\delta^{18}O$ and δD by repeatedly sampling two different working standards with known isotopic composition. At 100 ppmv we determined an accuracy of better than $3\permil$.

Dynamical tests with rapidly varying H_2O-mixing ratio between 40 ppmv and 1 000 ppmv as encountered in the upper troposphere have revealed randomly distributed shifts of the δ-values. These shifts arise from time dependent residual etalon structures, which are presently not well enough captured by our fit algorithm. While we are working on an improved algorithm we will also integrate a piezo-driven mirror into our multi-pass cell which should reduce the etalon signal considerably. At present the overall accuracy is limited to $\sim 50\permil$ for both $\delta^{18}O$ and δD at upper-tropospheric conditions.

In addition to its high sensitivity and good accuracy, the ISOWAT spectrometer is highly compact and lightweight. It is designed as a 19-inch subrack with a height of 35 cm and a mass of around 27 kg (excluding pump and calibration-gas source). The spectrometer is thus among the most compact airborne tunable-diode laser spectrometers. It is very well suited for airborne employment within the long-term passenger-aircraft project CARIBIC as well as aboard the new German high altitude research aircraft HALO. Within CARIBIC, scientific operation on four intercontinental flights per month will start presumably in December 2009. This platform is highly suitable to conduct long-term investigation of, e.g. tropospheric/stratospheric exchange. For operation aboard HALO, ISOWAT will be operated during two of the upcoming demonstration campaigns, namely *Mid Latitude Cirrus* (ML-CIRRUS) and *The Polar Stratosphere in a Changing Climate* (POLSTRACC).

(etalon signals), is the main limitation of both the precision and accuracy of our measurements. While for many molecules the spectral background can be recorded and subtracted when flushing the absorption cell with a gas without the target species [37, 41], this technique of background subtraction is not applicable to H_2O measurements due to the long exchange times caused by desorption of H_2O off the MPC and tubing walls. In a future version we will therefore implement a piezoelectric transducer to one of the multi-pass-cell mirrors in order to modulate the phase of the etalon signals. If modulated at a proper amplitude and frequency, this approach should minimize the etalon signals considerably [42]. It will thus improve both the short term precision as well as the accuracy of the spectrometer.

4 Summary and future perspectives

We have described the design and testing of the tunable diode-laser spectrometer ISOWAT which has been developed for airborne measurements of water-vapour isotope ratios $\delta^{18}O$ and δD. The spectrometer is based on wavelength-modulation spectroscopy employing second-derivative detection. Three individual absorption lines of $H_2^{16}O$, $H_2^{18}O$

References

1. W. Roedel, *Physik unserer Umwelt: Die Atmosphäre* (Springer, Berlin, 1992)
2. J.T. Houghton, Y. Ding, D.J. Griggs, M. Noguer, P.J. van der Linden, X. Dai, K. Maskell, C.A. Johnson (eds.), *Climate Change 2001: The Scientific Basis. Contribution of Working Group I to the Third Assessment Report of the Intergovernmental Panel on Climate Change (IPCC)* (Cambridge University Press, Cambridge, 2001)
3. D. Marsden, F.P.J. Valero, J. Atmos. Sci. **61**, 745 (2004)
4. H. Häckel, *Meteorologie* (Verlag Eugen Ulmer, Stuttgart, 2005)
5. E.J. Moyer, F.W. Irion, Y.L. Yung, M.R. Gunson, Geophys. Res. Lett. **23**, 2385 (1996)
6. A. Zahn, J. Atmos. Chem. **39**, 303 (2001)
7. R. Gonfiantini, Nature **271**, 534 (1978). http://www.nature.com/nature/journal/v271/n5645/pdf/271534a0.pdf
8. L. Merlivat, J. Chem. Phys. **69**, 2864 (1978)
9. H.A.J. Meijer, W.J. Li, Isot. Environ. Health Stud. **34**, 349 (1998)
10. V.H. Payne, D. Noone, A. Dudhia, C. Piccolo, R.G. Grainger, Q. J. R. Meteorol. Soc. **133**, 1459 (2007)
11. J. Steinwagner, M. Milz, T. von Clarmann, N. Glatthor, U. Grabowski, M. Höpfner, G.P. Stiller, T. Röckmann, Atmos. Chem. Phys. **7**, 2601 (2007). www.atmos-chem-phys.net/7/2601/2007/
12. P. Franz, T. Röckmann, Atmos. Chem. Phys. **5**, 2949 (2005). www.atmos-chem-phys.org/acp/5/2949/
13. J. Worden, K. Bowman, D. Noone, R. Beer, S. Clough, A. Eldering, B. Fisher, A. Goldman, M. Gunson, R. Herman, S.S. Kulawik, M. Lampel, M. Luo, G. Osterman, C. Rinsland, C. Rodgers, S. Sander, M. Shephard, H. Worden, J. Geophys. Res. **111**, D16309 (2006)
14. R. Nassar, P.F. Bernath, C.D. Boone, A. Gettelman, S.D. McLeod, C.P. Rinsland, J. Geophys. Res. **112**, D21305 (2007)
15. C.R. Webster, A.J. Heymsfield, Science **302**, 1742 (2003)
16. C.R. Webster, R.D. May, C.A. Trimble, R.G. Chave, J. Kendall, Appl. Opt. **33**, 454 (1994)
17. E. Kerstel, R. Iannone, M. Chenevier, S. Kassi, H.J. Jost, D. Romanini, Appl. Phys. B **85**, 397 (2006). doi:10.1007/s00340-006-2356-1
18. R.Q. Iannone, S. Kassi, H.J. Jost, M. Chenevier, D. Romanini, H.A.J. Meijer, S. Dhaniyala, M. Snels, E.R.T. Kerstel, Isot. Environ. Health Stud. **45**, 68–80 (2009). doi:10.1080/10256010903172715
19. T.F. Hanisco, E.J. Moyer, E.M. Weinstock, J.M.S. Clair, D.S. Sayres, J.B. Smith, R. Lockwood, J.G. Anderson, A.E. Dessler, F.N. Keutsch, J.R. Spackman, W.G. Read, T.P. Bui, Geophys. Res. Lett. **34**, 4814 (2007). doi:10.1029/2006GL027899
20. D.S. Sayres, E.J. Moyer, T.F. Hanisco, J.M.S. Clair, F.N. Keutsch, A. O'Brien, N.T. Allen, L. Lapson, J.N. Demusz, M. Rivero, T. Martin, M. Greenberg, C. Tuozzolo, G.S. Engel, J.H. Kroll, J.B. Paul, J.G. Anderson, Rev. Sci. Instrum. **80**, 044102 (2009). doi:10.1063/1.3117349. http://link.aip.org/link/?RSI/80/044102/1
21. J.M. St. Clair, T.F. Hanisco, E.M. Weinstock, E.J. Moyer, D.S. Sayres, F.N. Keutsch, J.H. Kroll, J.N. Demusz, N.T. Allen, J.B. Smith, J.R. Spackman, J.G. Anderson, Rev. Sci. Instrum. **79**, 064101 (2008). doi:10.1063/1.2940221. http://link.aip.org/link/?RSI/79/064101/1
22. E.J. Moyer, T.F. Hanisco, D.S. Sayres, J. St. Clair, F.N. Keutsch, N.T. Allen, L.R. Lapson, E.M. Weinstock, J.S. Smith, J.B. Paul, J.G. Anderson, in *Field Laser Applications in Industry and Research (FLAIR)* (Florence, Italy, 2007)
23. C.A.M. Brenninkmeijer, P. Crutzen, F. Boumard, T. Dauer, B. Dix, R. Ebinghaus, D. Filippi, H. Fischer, H. Franke, U. Frieß, J. Heintzenberg, F. Helleis, M. Hermann, H.H. Kock, C. Koeppel, J. Lelieveld, M. Leuenberger, B.G. Martinsson, S. Miemczyk, H.P. Moret, H.N. Nguyen, P. Nyfeler, D. Ora, D. O'Sullivan, S. Penkett, U. Platt, M. Pupek, M. Ramonet, B. Randa, M. Reichelt, T.S. Rhee, J. Rohwer, K. Rosenfeld, D. Scharffe, H. Schlager, U. Schumann, F. Slemr, D. Sprung, P. Stock, R. Thaler, F. Valentino, P. van Velthoven, A. Waibel, A. Wandel, K. Waschitschek, A. Wiedensohler, I. Xueref-Remy, A. Zahn, U. Zech, H. Ziereis, Atmos. Chem. Phys. **7**, 4953 (2007)
24. L. Rothman, I. Gordon, A. Barbe, D. Benner, P. Bernath, M. Birk, V. Boudon, L. Brown, A. Campargue, J.P. Champion, K. Chance, L. Coudert, V. Dana, V. Devi, S. Fally, J.M. Flaud, R. Gamache, A. Goldman, D. Jacquemart, I. Kleiner, N. Lacome, W. Lafferty, J.Y. Mandin, S. Massie, S. Mikhailenko, C. Miller, N. Moazzen-Ahmadi, O. Naumenko, A. Nikitin, J. Orphal, V. Perevalov, A. Perrin, A. Predoi-Cross, C. Rinsland, M. Rotger, M. Simecková, M. Smith, K. Sung, S. Tashkun, J. Tennyson, R. Toth, A. Vandaele, J.V. Auwera, J. Quant. Spectros. Radiat. Transfer **110**, 533 (2009). doi:10.1016/j.jqsrt.2009.02.013. http://www.sciencedirect.com/science/article/B6TVR-4VPM5M4-2/2/464a427cb2670a9be660fe6e0e4d0272. HITRAN
25. L. Gianfrani, G. Gagliardi, M. van Burgel, E.R.T. Kerstel, Opt. Express **11**, 1566 (2003)
26. E.R.T. Kerstel, R. van Trigt, N. Dam, J. Reuss, H.A.J. Meijer, Anal. Chem. **71**, 5297 (1999)
27. C. Dyroff, Tunable Diode-Laser Absorption Spectroscopy for Trace-Gas Measurements with High Sensitivity and Low Drift. Ph.D. thesis, University of Karlsruhe (TH), ISBN: 978-3-86644-328-0 (2009). http://digbib.ubka.uni-karlsruhe.de/volltexte/1000010030
28. C. Gurk, H. Fischer, P. Hoor, M.G. Lawrence, J. Lelieveld, H. Wernli, Atmos. Chem. Phys. **8**, 6395 (2008)
29. J.E. Collins, G.W. Sachse, B.E. Anderson, A.J. Weinheimer, J.G. Walega, B.A. Ridley, Geophys. Res. Lett. **20**, 2543 (1993)
30. S.E. Strahan, J. Geophys. Res. **104**, 30463 (1999)
31. E. Kerstel, *Handbook of Stable Isotope Analytical Techniques* (Elsevier, Amsterdam, 2004)
32. J.B. McManus, P.L. Kebabian, M.S. Zahniser, Appl. Opt. **34**, 3336 (1995)
33. K. Rößner, M. Hümmer, T. Lehnhardt, M. Müller, A. Forchel, IEEE Photonics Technol. Lett. **18**, 1424 (2006)
34. R.N. Hager Jr., R.C. Anderson, J. Opt. Soc. Am. **60**, 1444 (1970)
35. P. Werle, Spectrochim. Acta, Part A **54**, 197 (1998)
36. T. Iguchi, J. Opt. Soc. Am. **3**, 419 (1986)
37. P. Werle, P. Mazzinghi, F. D'Amato, M.D. Rosa, K. Maurer, F. Slemr, Spectrochim. Acta, Part A **60**, 1685 (2004)
38. M.F. Miller, Geochim. Cosmochim. Acta **66**, 1881 (2002). doi:10.1016/S0016-7037(02)00832-3
39. J.R. Gat, Annu. Rev. Earth Planet. Sci. **24**, 225 (1996)
40. D. Wagenbach, Personal communication (2008)
41. B.P. Wert, A. Fried, S. Rauenbuehler, J. Walega, B. Henry, J. Geophys. Res. **108**, 4350 (2003). doi:10.1029/2002JD002872
42. J.A. Silver, A.C. Stanton, Appl. Opt. **27**, 1914 (1988)